

The cold dark matter content of Galactic dwarf spheroidals: no cores, no failures, no problem

Azadeh Fattahi^{1*}, Julio F. Navarro^{1,2}, Till Sawala³, Carlos S. Frenk⁴,
Laura V. Sales⁵, Kyle Oman¹, Matthieu Schaller⁴ and Jie Wang⁵

¹*Department of Physics and Astronomy, University of Victoria, PO Box 3055 STN CSC, Victoria, BC, V8W 3P6, Canada*

²*Senior CIFAR Fellow.*

³*Department of Physics, University of Helsinki, Gustaf Hällströmin katu 2a, FI-00014 Helsinki, Finland*

⁴*Institute for Computational Cosmology, Department of Physics, University of Durham, South Road, Durham DH1 3LE, United Kingdom*

⁵*Department of Physics and Astronomy, University of California Riverside, 900 University Ave., CA92507, US*

⁶*Key laboratory for Computational Astrophysics, National Astronomical Observatories, Chinese Academy of Sciences, Beijing, 100012, China*

25 July 2016

ABSTRACT

We examine the dark matter content of satellite galaxies in Λ CDM cosmological hydrodynamical simulations of the Local Group from the APOSTLE project. We find excellent agreement between simulation results and estimates for the 9 brightest Galactic dwarf spheroidals (dSphs) derived from their stellar velocity dispersions and half-light radii. Tidal stripping plays an important role by gradually removing dark matter from the outside in, affecting in particular fainter satellites and systems of larger-than-average size for their luminosity. Our models suggest that tides have significantly reduced the dark matter content of Can Ven I, Sextans, Carina, and Fornax, a prediction that may be tested by comparing them with field galaxies of matching luminosity and size. Uncertainties in observational estimates of the dark matter content of individual dwarfs have been underestimated in the past, at times substantially. We use our improved estimates to revisit the ‘too-big-to-fail’ problem highlighted in earlier N-body work. We reinforce and extend our previous conclusion that the APOSTLE simulations show no sign of this problem. The resolution does *not* require ‘cores’ in the dark mass profiles, but, rather, relies on revising assumptions and uncertainties in the interpretation of observational data and accounting for ‘baryon effects’ in the theoretical modelling.

Key words: Cosmology – Local Group – galaxies:dwarf – galaxies:haloes – galaxies: kinematics and dynamics

1 INTRODUCTION

The steep slope of the dark matter halo mass function at the low-mass end is a defining characteristic of the Λ CDM cosmological paradigm. It is much steeper than the faint-end slope of the galaxy stellar mass function, implying that low-mass CDM haloes are significantly more abundant than faint dwarf galaxies (Moore et al. 1999; Klypin et al. 1999). This discrepancy is usually reconciled by assuming that dwarfs form preferentially in relatively massive haloes, because cosmic reionization and the energetic feedback from stellar evolution are effective at removing baryons from the

shallow gravitational potential of low-mass systems and at curtailing their star forming activity (Bullock et al. 2000; Benson et al. 2002; Somerville 2002).

Such scenario makes clear predictions for the stellar mass – halo mass relation at the faint end. A simple – but powerful and widely used – parameterization of this prediction is obtained from abundance matching (AM) modeling, where galaxies and CDM haloes are ranked by mass and matched to each other respecting their relative ranked order (see, e.g., Frenk et al. 1988; Vale & Ostriker 2004; Guo et al. 2011; Moster et al. 2013; Behroozi et al. 2013). Halo masses may thus be derived from stellar masses, yielding clear predictions amenable to observational testing.

Most such tests rely on using kinematic tracers such as

* Email: azadehf@uvic.ca

rotation speeds or velocity dispersions to estimate the total gravitational mass enclosed within the luminous radius of a galaxy. Its dark matter content, computed after subtracting the contribution of the baryons, may then be used to estimate the total virial¹ mass of the system. Such estimates rely heavily on the similarity of the mass profiles of CDM haloes (Navarro et al. 1996b, 1997, referred to hereafter as NFW), and involve a fairly large extrapolation, since virial radii are typically much larger than galaxy radii.

These tests have revealed some tension between the predictions of AM models and observations. Boylan-Kolchin et al. (2011), for example, estimated masses for the most luminous Galactic satellites that were lower than those of the most massive substructure haloes in N-body simulations of Milky Way-sized haloes from the Aquarius Project (Springel et al. 2008). Ferrero et al. (2012) reported a related finding when analyzing the dark matter content of faint dwarf irregular galaxies in the field: many of them implied total virial masses well below those predicted by AM models. Subsequent work has highlighted similar results both in the analysis of M31 satellites (Tollerud et al. 2014; Collins et al. 2014), as well as in other samples of field galaxies (Garrison-Kimmel et al. 2014; Papastergis et al. 2015).

These discrepancies may in principle be reconciled with Λ CDM in a number of ways. One possibility is to reconsider virial mass estimates based on the dark mass enclosed by the galaxy, a procedure that is highly sensitive to assumptions about the halo mass profile. A popular revision assumes that the assembly of the galaxy may lead to a reshuffling of the mass profile, pushing dark matter out of the inner regions and creating a constant-density ‘core’ in an otherwise cuspy NFW halo (e.g., Navarro et al. 1996a; Mashchenko et al. 2006; Governato et al. 2012).

These cores allow dwarf galaxies to inhabit massive haloes despite their relatively low inner dark matter content. This option has received some support from hydrodynamical simulations (see, e.g., Pontzen & Governato 2014, for a review) although the results are sensitive to how star formation and feedback are implemented. Indeed, no consensus has yet been reached over the magnitude of the effect, its dependence on mass, or even whether such cores exist at all (see, e.g., Parry et al. 2012; Garrison-Kimmel et al. 2013; Di Cintio et al. 2014; Schaller et al. 2015b; Oman et al. 2015; Oñorbe et al. 2015, and references therein).

A second possibility is that Galactic satellites have been affected by tidal stripping, which would preferentially remove dark matter (e.g., Peñarrubia et al. 2008b) and, therefore, act to reduce their dark mass content, much as the baryon-induced ‘cores’ discussed in the preceding paragraph. This proposal would not help to solve the issue raised by field dwarf irregulars (Ferrero et al. 2012) nor the low dark matter content of Galactic satellites (tides are, of course, already included in N-body halo simulations), unless baryon-induced cores help to enhance the effects of tides, as proposed by Zolotov et al. (2012) and Brooks & Zolotov (2014).

A third option is to revise the abundance matching prescription so as to allow dwarf galaxies to inhabit haloes of lower mass. This would be the case if some galaxies simply fail to form (or are too faint to feature in current surveys) in haloes below some mass: once these “dark” systems are taken into account, the AM stellar mass – halo mass relation would shift to systematically lower virial masses for given stellar mass, as pointed out by Sawala et al. (2013).

The existence of ‘dark’ subhaloes does not, on its own, solve the problem pointed out by Boylan-Kolchin et al. (2011), which is usually referred to as the ‘too-big-to-fail’ problem (hereafter TBTF, see also Boylan-Kolchin et al. 2012). Indeed, associating dwarfs with lower halo masses would not explain why many of the most massive substructures in the Aquarius haloes seem inconsistent with the kinematic constraints of the known Galactic satellites.

One explanation might be that fewer massive subhaloes are present in the Milky Way (MW) than in Aquarius haloes. Since the number of substructures scales with the virial mass of the main halo, a lower Milky Way mass would reduce the number of massive substructures, thus alleviating the problem (Wang et al. 2012; Vera-Ciro et al. 2013; Cautun et al. 2014). Another possibility is that dark-matter-only (DMO) simulations like Aquarius overestimate the subhalo mass function. Low mass haloes are expected to lose most of their baryons to cosmic reionization and feedback, a loss that stunts their growth and reduces their final mass. The effect is limited in terms of mass (baryons, after all, make up only 17 per cent of the total mass of a halo) but it can have disproportionate consequences on the number of massive substructures given the steepness of the subhalo mass function (Guo et al. 2015; Sawala et al. 2016).

We explore these issues here using Λ CDM cosmological hydrodynamical simulations of the Local Group from the APOSTLE² project (Fattahi et al. 2016; Sawala et al. 2016). These simulations use the same code as the EAGLE project, whose numerical parameters have been calibrated to reproduce the galaxy stellar mass function and the distribution of galaxy sizes (Schaye et al. 2015; Crain et al. 2015). Our analysis complements that of Sawala et al. (2016), who showed that APOSTLE reproduces the Galactic satellite luminosity/stellar mass function, as well as the total number of galaxies brighter than $10^5 M_{\odot}$ within the Local Group.

We extend here the TBTF discussion of that paper by reviewing the accuracy of observational constraints (Sec. 2), which are based primarily on measurements of line-of-sight velocity dispersions and the stellar half-mass radii ($r_{1/2}$) of ‘classical’ (i.e., $M_V < -8$) Galactic dwarf spheroidals (dSphs), and by focusing our analysis on the actual mass enclosed within $r_{1/2}$ rather than on extrapolated quantities such as the maximum circular velocity of their surrounding haloes. We also highlight the effect of Galactic tides, and identify the satellites where such effects might be more easily detectable observationally.

This paper is organized as follows. We begin by reviewing in Sec. 2 the observational constraints on the mass of Galactic dSphs. We then describe briefly our simulations and discuss our main results in Sec. 3, and conclude with a summary of our main conclusions in Sec. 4.

¹ We define virial quantities as those corresponding to the radius where the spherical mean density equals 200 times the critical density for closure, $3H^2/8\pi G$. Virial quantities are identified by a “200” subscript.

² A Project Of Simulating The Local Environment

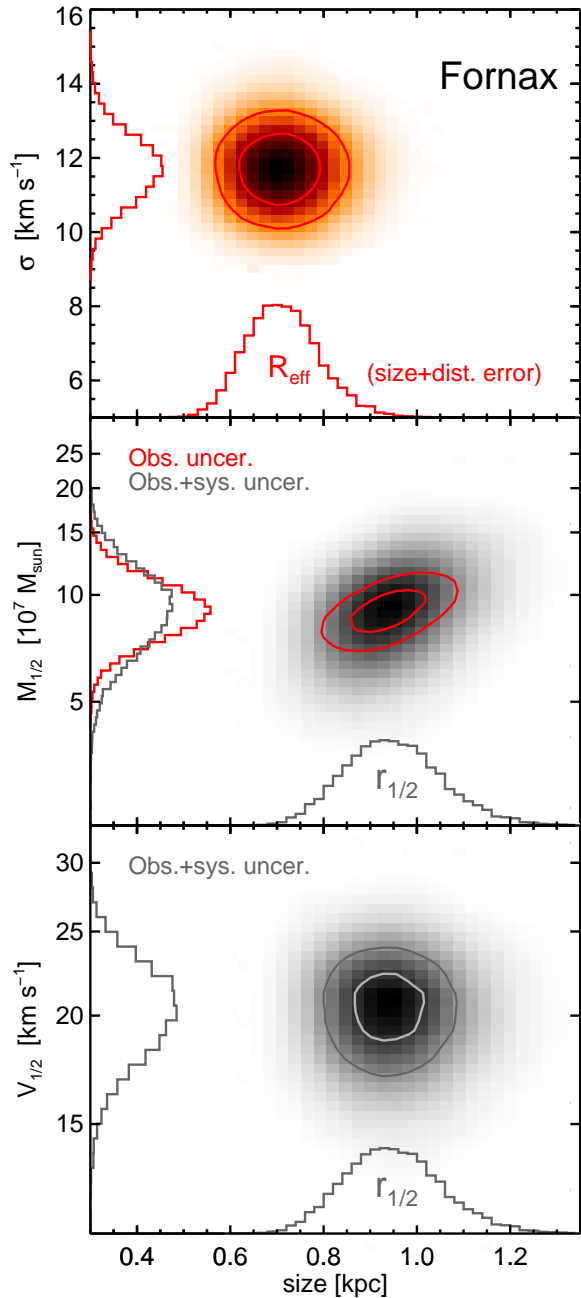


Figure 1. *Top:* Stellar velocity dispersion and effective radius (R_{eff}) of the Fornax dSph. The R_{eff} distribution is obtained by convolving uncertainties in distance and in the observed angular half-light radius, using uncertainties from the literature and assuming Gaussian error distributions. *Middle:* Dynamical mass within the deprojected 3D half-light radius ($r_{1/2}$) of Fornax, calculated using eq. 1 (Wolf et al. 2010). The red histogram shows the result of propagating the observational uncertainties, whereas the grey histogram adds a 23 per cent base modeling uncertainty, as suggested by Campbell et al. (2016). *Bottom:* Circular velocity at $r_{1/2}$ ($V_{1/2}$), including both observational and systematic uncertainties, calculated from the final $M_{1/2}$ distribution (middle panel). Unlike $M_{1/2}$, $V_{1/2}$ is independent of $r_{1/2}$. Contours in all panels enclose 50 per cent and 80 per cent of the distributions.

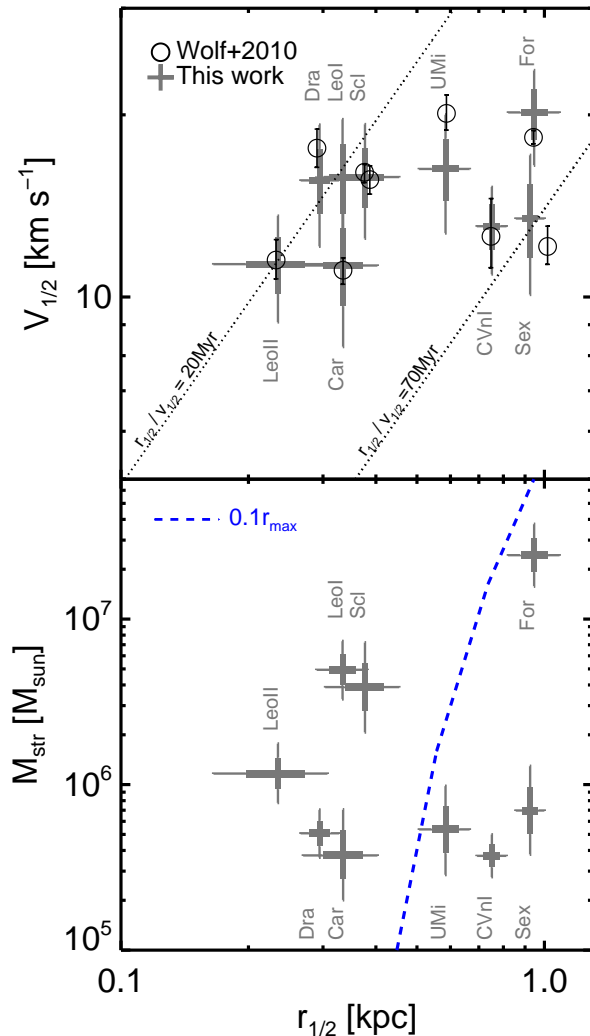


Figure 2. *Top:* Circular velocity at the half-light radius of Milky Way classical dSphs. Open circles show the results of Wolf et al. (2010) with 1σ error. The bar-and-whisker symbols show the results of this work, including observational and systematic uncertainties (see, e.g., the bottom panel of Fig. 1 for the case of the Fornax dSph). The thick and thin portions illustrate interquartile and 10–90th percentile intervals, respectively. Our results suggest that $V_{1/2}$ uncertainties have been underestimated in previous work. Slanted lines show objects with constant crossing time, as labelled. *Bottom:* Stellar mass derived for the 9 Galactic dSphs, shown as a function of their half-light radius. The blue dashed line indicates the characteristic halo mass – radius dependence of APOSTLE centrals, computed from the fit shown in Fig. 3. The line divides the sample in two groups of compact objects resilient to tides and more extended systems where tidal effects may be more apparent.

2 THE MASS OF MILKY-WAY DWARF SPHEROIDALS

Dwarf spheroidals (dSph) are dispersion-supported stellar systems, with little or no gaseous content. Their stellar velocity dispersion may be combined with the half-mass radius, $r_{1/2}$, to estimate the total mass enclosed within $r_{1/2}$. This estimate depends only weakly on the velocity

anisotropy, provided that the system is in equilibrium, close to spherically symmetric, and that its velocity dispersion is relatively flat (Walker et al. 2009a; Wolf et al. 2010). In that case, the latter authors show that the total mass enclosed within the (deprojected) half-mass radius is well approximated by

$$M_{1/2} = 3 G^{-1} \sigma_{\text{los}}^2 r_{1/2}, \quad (1)$$

where σ_{los} is the luminosity-weighted line-of-sight velocity dispersion of the stars and $r_{1/2}$ has been estimated from the (projected) effective radius, R_{eff} , using $r_{1/2} = (4/3)R_{\text{eff}}$.

The velocity dispersion profiles of the Milky Way classical dSph satellites are indeed nearly flat (Walker et al. 2007, 2009a), and eq. 1 has been used to estimate $M_{1/2}$ or, equivalently, the circular velocity at $r_{1/2}$, $V_{1/2} = \sqrt{GM_{1/2}/r_{1/2}}$, for many of them. The two parameters needed for eq. 1 are inferred from (i) individual stellar velocities; (ii) the angular projected half-light radius; and (iii) the distance modulus, each of which is subject to observational uncertainty. A lower limit on the uncertainty in $M_{1/2}$ may thus be derived by propagating the uncertainties in each of those three quantities. We shall adopt the most up-to-date values from the McConnachie (2012) Local Group compilation³ as the main source of observational data. Table A1 lists our adopted values for the 9 dSphs within 300 kpc from the Milky Way. (We have excluded the Sagittarius dwarf from our analysis because it is in the process of being tidally disrupted.)

We show in Fig. 1 the error budget (assumed Gaussian unless otherwise specified) for the case of the Fornax dSph, one of the best studied Galactic dSphs. The top panel illustrates the errors in σ_{los} and R_{eff} , including errors in the distance and the angular half size. The red histogram in the middle panel of Fig. 1 shows the result of applying eq. 1, after transforming R_{eff} into 3D $r_{1/2}$, assuming no additional error.

The error propagation results in a 30 per cent uncertainty in $M_{1/2}$, with some covariance with that in $r_{1/2}$. Note that this uncertainty is substantially larger than the ~ 7 per cent uncertainty quoted for Fornax by Wolf et al. (2010). Furthermore, the uncertainty shown by the red histogram in Fig. 1 assumes that applying eq. 1 introduces no additional error. This assumption has been recently examined by Campbell et al. (2016), who conclude that such modeling has a base systematic uncertainty of ~ 23 per cent, even when half-mass radii and velocity dispersions are known with exquisite accuracy. We therefore add this in quadrature to obtain the grey histogram in the middle panel of Fig. 1. Finally, using the circular velocity, $V_{1/2}$, instead of $M_{1/2}$ removes the covariance between mass and radius (see bottom panel of the same figure), so we shall hereafter adopt $V_{1/2}$ for our analysis.

We have followed this procedure to compute $r_{1/2}$ and $V_{1/2}$ for all 9 classical MW dSphs, and quote their values and uncertainties in Table A1. Note that in a number of cases these uncertainties are well in excess of those assumed in recent work. This may also be seen in the top panel of Fig. 2, where the grey crosses indicate our results and compare them with the values quoted by Wolf et al. (2010), shown by the open circles. Some of the differences may be ascribed to

revisions to the observational data from more recent studies and some to the increase in the error due to the base systematic uncertainty discussed above.

We have also estimated stellar masses for all Galactic dSphs in order to facilitate comparison with simulated data. We do this by using the V -band magnitude and distance modulus from the compilation of McConnachie (2012), and stellar mass-to-light ratios from Woo et al. (2008). Errors in V -band magnitude and distance modulus are taken from McConnachie (2012). Woo et al. (2008) do not provide uncertainties in the mass-to-light ratios, so we assume a constant 10 per cent uncertainty for all systems. We list all observable quantities and derived stellar masses in Table A1 and show, for future reference, the relation between stellar mass and half-mass radius in the bottom panel of Fig. 2.

3 RESULTS

3.1 The Local Group APOSTLE simulations

We shall use results from the APOSTLE project, a suite of cosmological hydrodynamical simulations of 12 independent volumes chosen to resemble the Local Group of Galaxies (LG), with a relatively isolated dominant pair of luminous galaxies analogous to M31 and the Milky Way. A full description of the volume selection procedure and of the simulations is presented in Fattahi et al. (2016) and Sawala et al. (2016). We briefly summarize here the main parameters of the simulations relevant to our analysis.

LG candidate volumes for resimulation were selected from a dark-matter-only (DMO) simulation of a $(100 \text{ Mpc})^3$ cosmological box with 1620^3 particles (known as DOVE, Jenkins 2013). DOVE adopts cosmological parameters consistent with 7-year *Wilkinson Microwave Anisotropy Probe* (WMAP-7, Komatsu et al. 2011) measurements, as follows: $\Omega_m = 0.272$, $\Omega_\Lambda = 0.728$, $h = 0.704$, $\sigma_8 = 0.81$, $n_s = 0.967$.

Each APOSTLE volume includes a relatively-isolated pair of haloes with kinematics consistent with the MW–M31 pair; in particular: (i) the pair members are separated by 600 to 1000 kpc; (ii) they are approaching each other with velocities in the range $(-250, 0) \text{ km s}^{-1}$; and (iii) their relative tangential velocities do not exceed 100 km s^{-1} . The virial mass of the pair members are in the range $(5 \times 10^{11}, 2.5 \times 10^{12}) M_\odot$, and the combined virial masses are in the range $(1.6 \times 10^{12}, 4 \times 10^{12}) M_\odot$. An isolation criterion is also adopted to ensure that no halo more massive than the smaller of the pair is found within 2.5 Mpc from the pair barycentre.

APOSTLE volumes were resimulated using the code developed for the EAGLE simulation project (Schaye et al. 2015; Crain et al. 2015). The code is a highly modified version of the Tree-PM/SPH code, P-Gadget3 (Springel 2005; Schaller et al. 2015a), with subgrid implementations for star formation, radiative cooling, metal enrichment, uniform UV and X-ray background (cosmic reionization), feedback from evolving stars, as well as the formation and growth of supermassive black holes and related feedback. APOSTLE runs use the parameters of the ‘Ref’ model described in Schaye et al. (2015). The EAGLE galaxy formation model has been calibrated to reproduce the galaxy stellar mass function and sizes in the mass range 10^8 – $10^{11} M_\odot$ at $z = 0.1$.

³ http://www.astro.uvic.ca/~alan/Nearby_Dwarf_Database.html

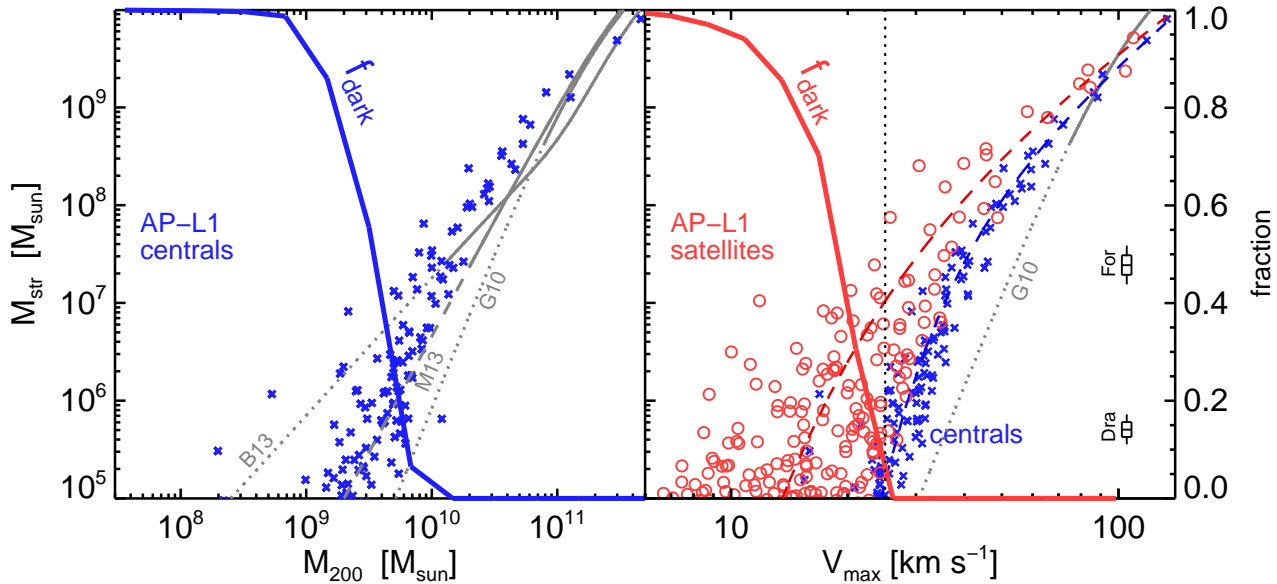


Figure 3. *Left:* Stellar mass – halo mass relation for ‘central’ galaxies in the highest resolution APOSTLE runs (L1). The abundance matching relations of Guo et al. (2010), Moster et al. (2013) and Behroozi et al. (2013) are shown for reference, labelled as G10, M13, and B13, respectively. The dotted portion of these curves indicates extrapolation of their formulae to low masses. The fraction of ‘dark’ systems in APOSTLE (i.e., no star particles) as a function of virial mass is indicated by the curve labelled ‘ f_{dark} ’, with the scale shown on the right axis. *Right:* Stellar mass versus maximum circular velocity (V_{max}) of centrals and satellite galaxies (at $z = 0$ for both) in APOSTLE, shown as blue crosses and red circles, respectively. The offset between field and satellite galaxies is due to loss of mass, mostly dark matter, caused by tidal stripping. The fraction of ‘dark’ subhaloes is shown by the solid red curve. There are no dark subhaloes with $V_{\text{max}} > 25 \text{ km s}^{-1}$. Blue and red dashed lines are fits to the central and satellite stellar mass – V_{max} relations, respectively, of the form $M_{\text{str}}/M_{\odot} = M_0 \nu^{\alpha} \exp(-\nu^{\gamma})$, where ν is the velocity in units of 50 km s^{-1} . Best fits have (M_0, α, γ) equal to $(3.0 \times 10^8, 3.36, -2.4)$ and $(8.0 \times 10^8, 2.70, -1.3)$ for centrals and satellites, respectively. For illustration, we indicate the stellar mass of Fornax and Draco with box-and-whisker symbols, at an arbitrary value of V_{max} .

This leads to relatively ‘flat’ rotation curves for luminous galaxies that agree well with observations (Schaller et al. 2015b).

The APOSTLE project aims to simulate each volume at three different resolution levels (L1 to L3). At the time of writing, all 12 APOSTLE volumes (AP-1 to AP-12) have been resimulated at L3 and L2 resolution levels with gas particle mass of $\sim 10^6 M_{\odot}$ and $\sim 10^5 M_{\odot}$, respectively. Three volumes (AP-1, AP-4, AP-11, see Fattahi et al. 2016) have also been completed at the highest resolution level, L1, with gas particle mass of $\sim 10^4$, DM particle mass of $\sim 5 \times 10^4 M_{\odot}$, and maximum gravitational softening of 134 pc. In this paper, we shall use mainly results from the APOSTLE L1 runs, unless otherwise specified.

Dark matter haloes in APOSTLE are identified using a friends-of-friends (FoF, Davis et al. 1985) algorithm with linking length equal to 0.2 times the mean interparticle separation. The FOF algorithm is run on the dark matter particles; gas and star particles acquire the FoF membership of their nearest DM particle. Self-bound substructures inside each FoF halo are then found recursively using the SUBFIND algorithm (Springel et al. 2001; Dolag et al. 2009). We will hereafter refer to the main structure of each FoF halo as its ‘central’, and to the self-bound substructures as its ‘satellites’. MW and M31 analogues in the simulations are referred to as primary galaxies.

3.2 Stellar mass – halo mass relation in APOSTLE

Abundance matching models provide the relation between the stellar mass and virial mass of galaxies by assuming that every dark matter halo hosts a galaxy and that there is a monotonic correspondence between stellar mass and halo mass. The relation is best specified in the regime where the galaxy stellar mass function is well determined ($M_{\text{str}} > 10^7 M_{\odot}$), but is routinely extrapolated to lower masses, usually assuming a power-law behaviour (Guo et al. 2010; Behroozi et al. 2013; Moster et al. 2013, hereafter G10, B13, and M13, respectively).

We compare the APOSTLE stellar mass – halo mass relation with the predictions of three different AM models in the left panel of Fig. 3. Stellar masses, M_{str} , are measured for simulated galaxies within the ‘galactic radius’, r_{gal} , defined as 0.15 times the virial radius the halo. This radius contains most of the stars and cold, star-forming gas of the main (‘central’) galaxy of each FoF halo. When considering galaxies inhabiting subhaloes (‘satellites’), whose virial radii are not well defined, we shall compute r_{gal} using their maximum circular velocity, V_{max} , after calibrating the $V_{\text{max}}-r_{\text{gal}}$ relation⁴ of the centrals.

The left panel of Fig. 3 shows that APOSTLE centrals do not form ‘stochastically’ in low mass haloes as envisioned

⁴ Specifically, we used $r_{\text{gal}}/\text{kpc} = 0.169 (V_{\text{max}}/\text{km s}^{-1})^{1.01}$

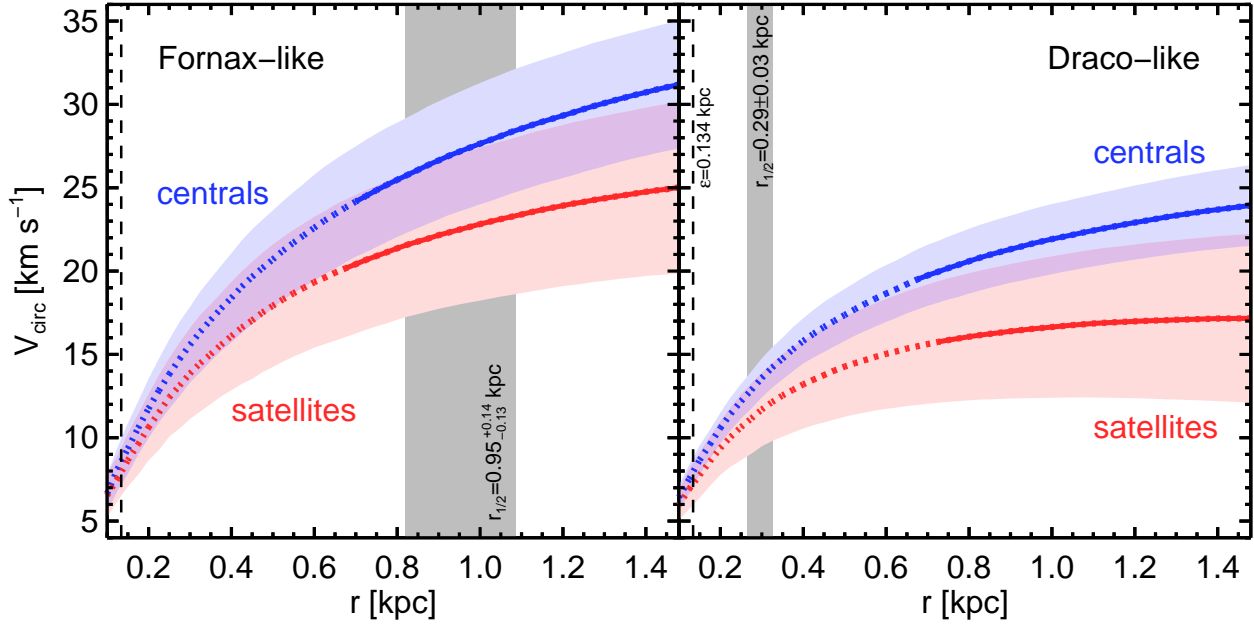


Figure 4. Circular velocity profiles of Fornax- and Draco-like satellites (red) and centrals (blue), as labelled. The solid lines indicate the average profiles, which turn to dotted inside the Power et al. (2003) convergence radius. Shaded regions indicate $\pm 1\sigma$ deviations. The grey vertical bars bracket the 10th and 90th percentiles of the half-light radii of Fornax and Draco, respectively. Note that, although both sets of satellites have been heavily stripped, the dark matter content within $r_{1/2}$ has been more significantly affected in the case of Fornax, given its relatively large size.

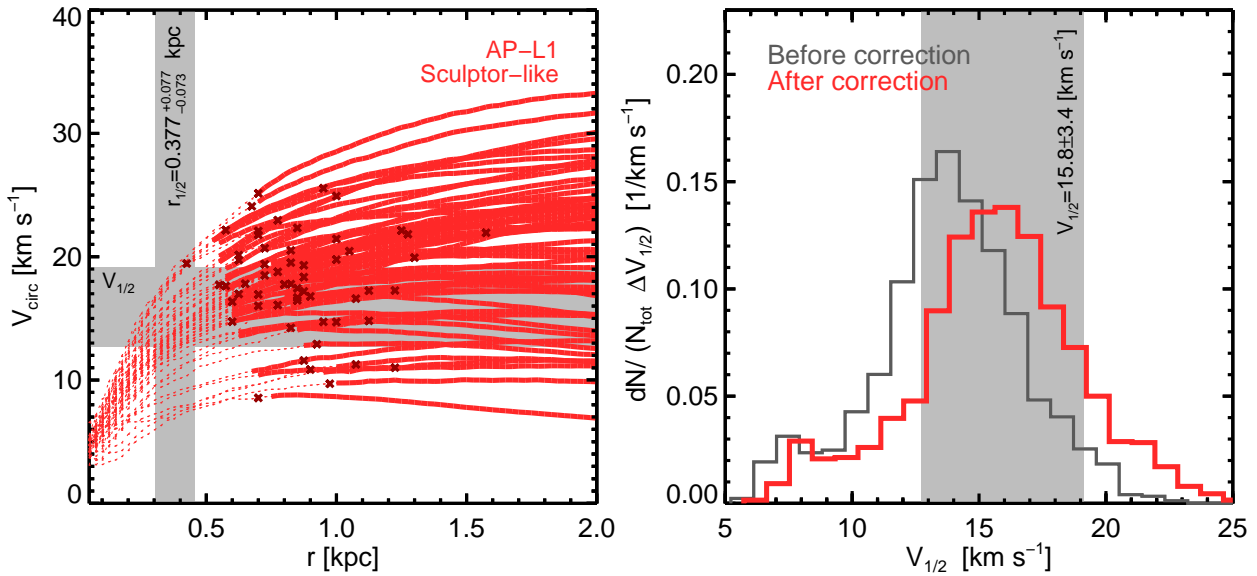


Figure 5. *Left:* Circular velocity curves of Sculptor-like satellites in APOSTLE, i.e., systems within 300 kpc from either of the main primaries with stellar mass matching that of Sculptor within 3σ of the central value given in Table A1. Curves turn from solid to dotted inside the Power et al. (2003) convergence radius (for $\kappa = 0.6$, see Appendix A). The grey vertical band indicates the half-light radius of Sculptor and the corresponding 10–90th percentile interval. Small crosses indicate the half-mass radii of Sculptor-like simulated satellites. *Right:* Distribution of circular velocities of Sculptor-like satellites, measured at the half-light radius of the Sculptor dSph (grey band on left). The red histogram shows the distribution after applying the resolution correction described in Appendix A. The grey vertical band corresponds to $V_{1/2}$ of Sculptor (10–90th percentile interval).

in some models (e.g., Guo et al. 2015), but, rather, follow a tight stellar mass – halo mass relation that deviates systematically from the AM predictions/extrapolations of G10 and M13. APOSTLE galaxies of given stellar mass live in haloes systematically less massive than extrapolated by those models but more massive than the B13 extrapolation. This reflects the fact that the galaxy stellar mass function of faint galaxies is rather poorly known, and that AM ‘predictions’ must be considered with care in this mass regime.

The systematic offset between the G10 and M13 AM extrapolations and our numerical results has been discussed by Sawala et al. (2013, 2015), who trace the disagreement at least in part to the increasing prevalence of ‘dark’⁵ haloes with decreasing virial mass. The effect of these dark systems is not subtle, as shown by the thick solid blue line in Fig. 3. This indicates the fraction of APOSTLE haloes that are dark (scale on right axis); only *half* of $10^{9.5} M_{\odot}$ haloes harbor luminous galaxies in APOSTLE. The ‘dark’ fraction increases steeply with decreasing mass: 9 out of 10 haloes with $M_{200} = 10^9 M_{\odot}$ are dark, and fewer than 1 in 50 haloes with virial mass $\sim 10^{8.8} M_{\odot}$ are luminous.

One might fear that the deviation from the AM prediction shown in Fig. 3 might lead to a surplus of faint galaxies in the Local Group. This is not the case; as discussed by Sawala et al. (2016), APOSTLE volumes contain ~ 100 galaxies with $M_{\text{str}} > 10^5 M_{\odot}$ within 2 Mpc from the LG barycentre, only slightly above the ~ 60 known such galaxies in the compilation of McConnachie (2012), which might still be incomplete due to the difficulty of finding dwarf galaxies in the Galactic ‘zone of avoidance’. We shall hereafter adopt $10^5 M_{\odot}$ (which corresponds roughly to a magnitude limit of $M_V \sim -8$) as the minimum galaxy stellar mass we shall consider in our discussion. In APOSTLE L1 runs these systems inhabit haloes of $M_{200} \sim 2 \times 10^9 M_{\odot}$ (three quarters of which are ‘dark’), and are resolved with a few tens of thousands of particles.

3.3 Tidal stripping effects

The right-hand panel of Fig. 3 is analogous to the left but using V_{max} (at $z = 0$) as a measure of mass (see also Sales et al. 2016). This allows the satellites in APOSTLE (open circles) to be included and compared with centrals (blue crosses). Satellites clearly deviate from centrals and push the offset from the G10 abundance matching prediction even further. This is mainly the result of tidal stripping, which affects disproportionately the dark matter content of a galaxy, reducing its V_{max} and increasing its scatter at a given stellar mass (see, e.g., Peñarrubia et al. 2008b, and references therein).

Despite the large scatter, a few results seem robust. One is that *every* subhalo with $V_{\text{max}} > 25 \text{ km s}^{-1}$ is host to a satellite more massive than $10^5 M_{\odot}$. This implies that the number of massive subhaloes provides a firm lower limit to the total number of satellites at least as bright as the ‘classical’ dSphs, an issue to which we shall return below.

A second point to note is that the effects of tidal stripping increase with decreasing stellar mass. Indeed, the V_{max}

of Fornax-like⁶ centrals is, on average, only 37 per cent higher than that of corresponding satellites; the difference, on the other hand, increases to 67 per cent in the case of Draco. This trend arises because dynamical friction erodes the orbits of massive satellites much faster than those of less luminous systems, leading to rapid merging or full disruption. As a result, surviving luminous satellites have, on average, been accreted more recently and have been less stripped than fainter systems (see, e.g., Barber et al. 2014).

This does not necessarily imply that the *stellar* components of fainter satellites have been more affected by stripping. Tides are more effective at removing (mostly dark) mass from the outskirts of a subhalo than from the inner regions, so their effects on the stellar component (for a given orbit) will be sensitive to the size of the satellite. This may be appreciated from Fig. 4, where we show the average circular velocity profiles of both Fornax- and Draco-like satellites and centrals. The outer regions are clearly more heavily stripped, implying that satellites that are physically large for their luminosity should show clearer signs of stripping than their more compact counterparts.

In other words, dSphs like Can Ven I or Sextans, for example, are much more likely to have been affected by tides than Draco or Leo II. Fig. 2 illustrates this in two different ways. In the top panel, the latter are seen to have much shorter crossing times than the former, making them more resilient to tides. Similarly, in the bottom panel, the former are shown to be physically larger than the latter both at fixed stellar mass and in terms of the characteristic radius of their host haloes (according to the stellar mass – halo mass relation for APOSTLE centrals shown in Fig. 3; see blue dashed line).

Thus, although our results suggest that satellites and field galaxies of similar M_{str} are expected to inhabit haloes of different V_{max} , the difference might not translate directly into an observable deficit in their dark matter content⁷. This is because V_{max} is usually reached at radii much larger than the stellar half-mass radii where kinematic data provide meaningful constraints. Given the large scatter in V_{max} at a given stellar mass shown by APOSTLE satellites, it is important to compare simulations and observations *at the same radii*. We explore this next.

3.4 The dark matter content of APOSTLE satellites

Our main conclusion from Fig. 3 is that APOSTLE satellites of given stellar mass are significantly less massive than expected from abundance matching and, because of stripping, span a relatively wide range of maximum circular velocities. Are these results consistent with the observational constraints discussed in Sec. 2? In other words, are the predicted values of $r_{1/2}$ and $V_{1/2}$ consistent with those of Galactic satellites of matching stellar mass?

⁶ We match Galactic satellites with APOSTLE dwarfs by stellar mass. For example, we refer to systems as Fornax-like if their M_{str} match Fornax’s within 3σ . Fornax-like *satellites* are those within 300 kpc of any of the APOSTLE primaries; Fornax-like *centrals* refer to field galaxies beyond that radius.

⁷ Indeed, Kirby et al. (2014) argue that no large differences seem to exist between field and satellite galaxies in the LG.

⁵ These are systems with no stars in APOSTLE L1, or, more precisely, $M_{\text{str}} < 10^4 M_{\odot}$, the mass of a single baryonic particle.

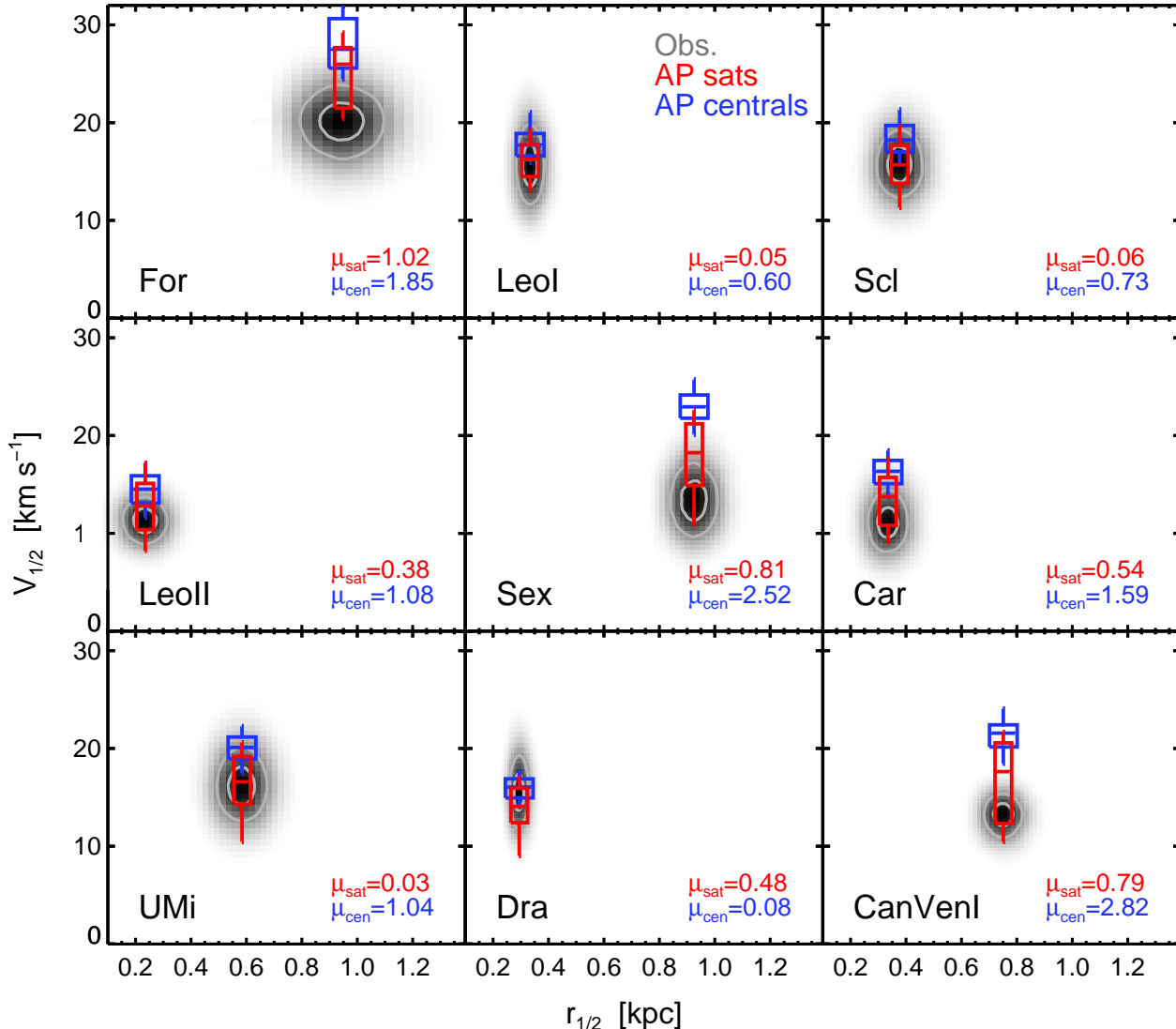


Figure 6. Circular velocity, $V_{1/2}$, of APOSTLE satellites matching the stellar mass of each of the 9 Galactic dSphs, and measured at the observed half-light radius of each system. Observational estimates and uncertainties are given by the grey cloud, whereas red bar-and-whisker symbols indicate the values for matching APOSTLE satellites. Contours indicate the regions containing 50 per cent and 80 per cent of the distributions. Bars and whiskers represent the interquartile and 10–90th percentile intervals of predicted $V_{1/2}$, plotted at the median value of $r_{1/2}$. Note the significant overlap between the satellite simulation results and the observational estimates; this may be quantified by the velocity difference between the mean observed and simulated values, divided by the combined rms of each distribution (μ), which is less than unity in all cases. The values of $V_{1/2}$ for APOSTLE centrals are larger, since centrals have not experienced tidal stripping.

The main issue to consider when addressing this question is that the half-light radii, $r_{1/2}$, of the faintest dSphs are smaller than the smallest well-resolved radius in APOSTLE. This impacts the analysis in two ways: one is that the faintest simulated dwarfs have radii larger than observed⁸; another is that the total mass enclosed by simulated dwarfs within radii as small as the observed half-light radii might be systematically affected by the limited resolution.

⁸ The subgrid equation of state imposed on star-forming gas particles by the EAGLE model results in a minimum effective radius of ~ 400 pc for galaxies in AP-L1 runs (see, e.g., Crain et al. 2015; Campbell et al. 2016).

We illustrate this in the left panel of Fig. 5 for the case of the Sculptor dSph. The vertical shaded band shows the half-light radius of that galaxy, $r_{1/2} = 377^{+77}_{-73}$ pc (10–90th percentile interval), whereas the small crosses indicate the stellar half-mass radii of Sculptor-like APOSTLE satellites on their circular velocity profiles, $V_{\text{circ}}(r)$. Clearly, for the comparison with Sculptor to be meaningful, we should estimate masses within the *observed* radius (grey band), rather than at the half-mass radius of each of the simulated systems.

However, the observed $r_{1/2}$ (although significantly larger than the gravitational softening, which is fixed at 134 pc at $z=0$ in AP-L1 runs) is smaller the minimum resolved

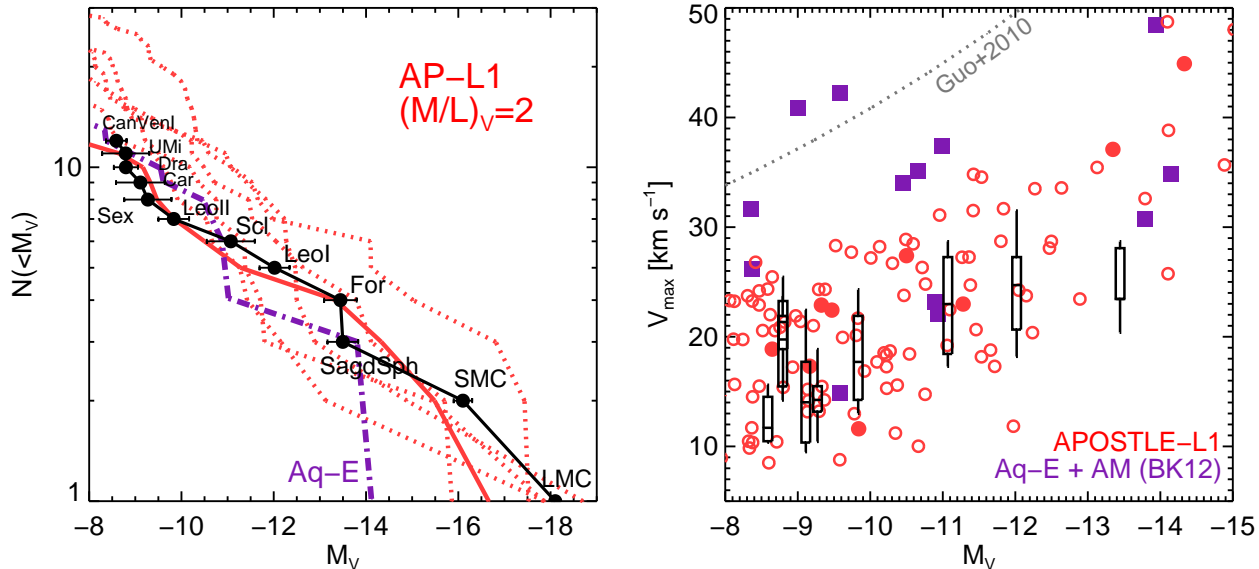


Figure 7. *Left:* Luminosity function of satellites of the six APOSTLE L1 primaries (dotted lines), compared with that of Galactic satellites (filled circles). We consider as satellites all systems within 300 kpc of the centre of each primary galaxy. We also show the luminosity function of the Aq-E halo (dot-dashed line) derived by Boylan-Kolchin et al. (2012) using an abundance matching model. The best fitting APOSTLE galaxy is highlighted with a solid line type. *Right:* V_{\max} - M_V relation for APOSTLE satellites (circles) compared with the abundance matching estimates for Aq-E subhaloes from Boylan-Kolchin et al. (2012). Box-and-whisker symbols indicate the V_{\max} range of APOSTLE satellites that match the stellar mass and $V_{1/2}$ of each of the 9 Galactic dSphs (see Sec. 3.5 for details). APOSTLE satellites inhabit markedly lower mass haloes than expected from abundance matching, at a given luminosity. APOSTLE also differs from Aq-E in the number of massive substructures. On average, each APOSTLE primary has ~ 7.2 satellite more massive than $V_{\max} > 25$ km s⁻¹; this number is actually only 5 for the halo that best matches the MW satellite luminosity function (solid circles; two of them are brighter than $M_V = -15$). Aq-E has 21 satellites with V_{\max} exceeding 25 km s⁻¹, some of them fainter than $M_V = -8$.

radius according to the convergence criterion proposed by Power et al. (2003). This is shown by the circular velocity profiles in Fig. 5, where the line types change from solid to dotted at the convergence radius, r_{conv} (defined by setting $\kappa = 0.6$ in eq. A2). The total mass within $r_{1/2}$ and, consequently, $V_{1/2}$, are therefore probably underestimated in the simulations. Fortunately, the analysis of Power et al. (2003) also shows that mass profiles inside r_{conv} deviate from convergence in a predictable fashion, so that a correction procedure is straightforward to devise and implement, at least for radii not too far inside r_{conv} .

In Appendix A, we describe the correction used to estimate the total mass enclosed within the Sculptor half-light radius for all Sculptor-like satellites in APOSTLE. The right-hand panel of Fig. 5 shows the APOSTLE $V_{1/2}$ estimates with and without correction. These estimates are obtained by randomly sampling the allowed range in $r_{1/2}$ as well as the $V_{\text{circ}}(r_{1/2})$ distribution of Sculptor-like APOSTLE satellites. In brief, this procedure involves: (i) choosing a random value for $r_{1/2}$ consistent with propagating the Gaussian errors in distance modulus and angular size (see Sec. 2 and col. 7 of Table A1); (ii) measuring $V_{1/2} = V_{\text{circ}}(r_{1/2})$ for a random satellite in AP-L1; and (iii) weighting⁹ each APOSTLE satellite by how closely it matches Sculptor’s stellar mass. (Although the procedure considers

all satellites, in practice only Sculptor-like satellites contribute meaningfully, given the weighting procedure.)

The procedure is repeated 10,000 times to derive the $V_{1/2}$ distribution shown in Fig. 5, which is then corrected for resolution as described in Appendix A. In the case of Sculptor the correction to the measured $V_{1/2}$ values is relatively mild; the median $V_{1/2}$ shifts only slightly, from 13.9 km s⁻¹ before correction to 15.7 km s⁻¹. This is actually the case for the majority of systems; the largest correction is obtained for the Leo II dSph, where the median $V_{1/2}$ increases by 24 per cent, from 10.3 km s⁻¹ to 12.8 km s⁻¹. Satellites like Fornax, which have larger half-light radii well-resolved by APOSTLE, are corrected by less than 5 per cent.

We apply the same procedure outlined above to all 9 Galactic ‘classical’ dSph satellites (excluding Sagittarius) and compare our results with observational constraints in Fig. 6. The grey shaded regions and contours denote the observational estimates including uncertainties, while the red box-and-whisker symbols indicate the results for APOSTLE satellites. There is clearly substantial overlap between observational estimates of $V_{1/2}$ and the APOSTLE results for all 9 dSphs, with no exception.

The values of μ_{sat} quoted in the legends of Fig. 6 indicate the absolute value of the difference between the mean observed and simulated values, in units of the combined rms: the difference is clearly not significant (less than unity) in any of the 9 cases. We conclude that the dark matter content of APOSTLE satellites is in good agreement with the observed values. We emphasize that this agreement is *not* the result of cored DM density profiles, as dwarf galaxies in

⁹ The weighting function is $\exp(-x^2/2\sigma^2)$, where $x = M_{\text{str}}^{\text{AP}} - M_{\text{str}}^{\text{Scl}}$, and σ is the uncertainty in Sculptor’s stellar mass discussed in Sec. 2.

APOSTLE show no evidence for cores (Oman et al. 2015; Sawala et al. 2016).

We may assess the effect of tidal stripping on our conclusion by repeating the above procedure using APOSTLE centrals, rather than satellites, for the comparison. The results are shown by the blue box-and-whisker symbols in Fig. 6 (red and blue boxes are plotted with different widths, for clarity). The values of $V_{1/2}$ are systematically larger for centrals, since they have not experienced tidal stripping. The agreement is clearly poorer, in particular for satellites ‘unusually large for their luminosities’ (Sec. 3.3) like Can Ven I, Sextans, Carina, and Fornax.

Consistency between APOSTLE and Galactic satellites therefore requires that the dark matter content of at least some dSphs has been affected by tides from the Milky Way halo. We emphasize that *all* subhaloes have been affected by tides; their effects, however, are noticeable mainly in systems whose sizes are large enough for their kinematics to probe regions where the mass loss is significant. The strong dependence of the effect of tides on galaxy size must be taken carefully into account when comparing the dynamics of satellite and isolated field galaxies to search for signs of environmental effects (see, e.g., Kirby et al. 2014).

3.5 The too-big-to-fail problem revisited

The previous section demonstrates that there is no conflict between the dark matter content of APOSTLE satellites and that of Galactic dSphs. This does not *per se* solve the ‘too-big-to-fail’ problem laid out by Boylan-Kolchin et al. (2011, 2012), which asserts that there is an excess of massive subhaloes without a luminous counterpart in Milky Way-sized haloes. Does this problem persist in APOSTLE?

We have examined this question earlier in Sawala et al. (2016), but we review those arguments here in light of the revised uncertainties in the mass of the Galactic classical dwarf spheroidals discussed in Sec 2. Fig. 7 reproduces the argument given by Boylan-Kolchin et al. (2012). The solid squares in the right-hand panel of our Fig. 7 are taken directly from their Fig. 6 and show the maximum circular velocities of the 13 most luminous subhaloes in the Aq-E halo, selected because, according to an abundance matching model patterned after Guo et al. (2010), its number of satellites brighter than $M_V = -8$ matches that of the Milky Way. This is shown by the magenta dot-dashed line in the left-hand panel of Fig. 7. The offset between the Aq-E solid squares and the Guo et al. (2010) prediction (dotted line on right-hand panel) is mainly due to tidal stripping.

Our APOSTLE L1 simulations also reproduce well the MW satellite luminosity function (see dotted lines in left-hand panel), but they differ from the Boylan-Kolchin et al. (2012) analysis of Aq-E in two respects. One is that our subhaloes are, on average, significantly less massive, at a given M_V , than assumed for Aq-E. This is because the APOSTLE stellar mass – halo mass relation is offset from abundance matching predictions (see Fig. 3).

The box-and-whisker symbols in the right-hand panel of Fig. 7 show the V_{\max} values (Table A2) of APOSTLE satellites that best match the stellar mass *and* $V_{1/2}$ of each Galactic dSph. The procedure for estimating V_{\max} is the same as that outlined in Sec. 3.4 for computing $V_{1/2}$ but, in addition, weights each simulated satellite by how closely it

matches the observed $V_{1/2}$. These new V_{\max} estimates complement and extend those reported by Sawala et al. (2016).

The second difference concerns the number of massive substructures: Aq-E has 21 subhaloes with $V_{\max} > 25 \text{ km s}^{-1}$ within 300 kpc from the centre, 10 of which are more luminous than $M_V = -8$, according to the model of Boylan-Kolchin et al. (2012). On the other hand, APOSTLE L1 primaries have, on average, just 7.2 ± 2.5 subhaloes with $V_{\max} > 25 \text{ km s}^{-1}$ within the same volume. Indeed, the APOSTLE primary whose satellite population best matches the MW satellite luminosity function (solid red curve in the left-panel of Fig. 7) has only 5 subhaloes this massive, as indicated by the solid circles in the right-hand panel of the same figure. (Two of those host satellites brighter than $M_V = -15$.)

As discussed by Sawala et al. (2016), the reason for the discrepancy is twofold. (i) Subhalo masses are systematically lower in cosmological hydrodynamical simulations because of the reduced growth brought about by the early loss of baryons caused by cosmic reionization and feedback. This reduces the V_{\max} of all subhaloes by ~ 12 per cent. (ii) Chance plays a role too, as Aq-E seems particularly rich in massive substructures. The average number of subhaloes with $V_{\max} > 25 \text{ km s}^{-1}$ expected *within the virial radius* of a halo of virial mass $M_{200} = 1.2 \times 10^{12} M_\odot$ is just 8.1 (Wang et al. 2012), compared with 18 for Aq-E, a $> 3\sigma$ upward fluctuation. Note that the expected number would drop to just 5.4 after correcting for the ~ 12 per cent reduction in V_{\max} . Indeed, the subhalo velocity function is so steep that even a slight variation in V_{\max} leads to a disproportionately large change in the number of massive substructures.

The discrepancy between APOSTLE and Aq-E noted above can therefore be ascribed to a chance upward fluctuation in the number of massive substructures in Aq-E coupled with the reduction of subhalo masses due to the loss of baryons in a hydrodynamical simulation.

3.6 TBTF and the mass of the Milky Way

The number of massive substructures is, of course, quite sensitive to the virial mass of the host halo. Following Wang et al. (2012) and Cautun et al. (2014), we may use this to derive an upper limit to the mass of the Milky Way. In APOSTLE every subhalo with $V_{\max} > 25 \text{ km s}^{-1}$ hosts a satellite brighter than $M_V = -8$ (or, equivalently, more massive than $M_{\text{str}} \sim 10^5 M_\odot$; see the right-hand panel of Fig. 3). This means that any potential Milky Way host halo with more than ~ 12 subhaloes this massive will either suffer from a ‘too-big-to-fail’ problem or have an excess of luminous satellites.

We examine this in Fig. 8, which shows the number of massive subhaloes within r_{200} as a function of virial mass. The criterion above implies that, in the top panel, only systems below the dashed line labelled ‘MW’ are likely to reproduce well the MW satellite population. The grey band in the same panel shows the expected number ($\pm 1\sigma$) of massive substructures according to Wang et al. (2012). Small (grey) open circles indicate the results from a 752^3 -particle dark-matter-only simulation of a cube 25 Mpc on a side. Small (green) filled circles correspond to the same volume, but for a run including baryons and the full galaxy forma-

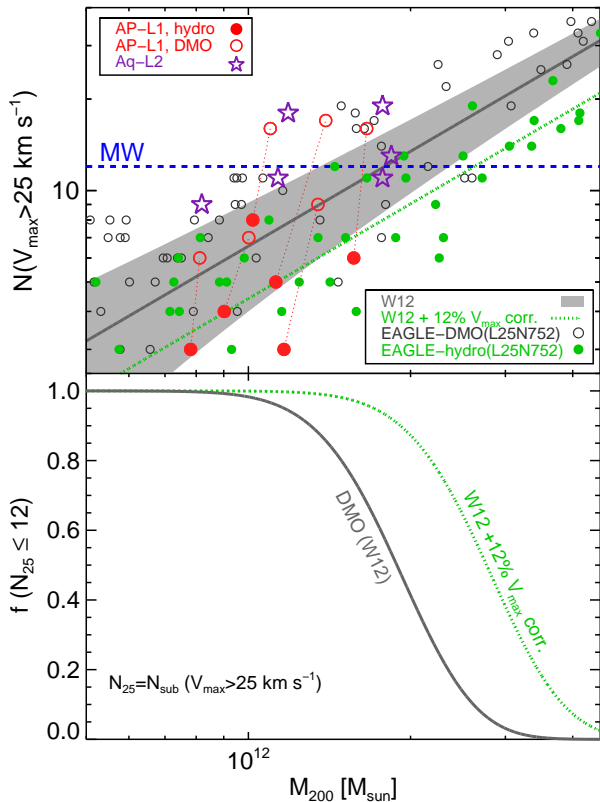


Figure 8. *Top:* Number of massive subhaloes ($V_{\max} > 25 \text{ km s}^{-1}$) within r_{200} , shown as a function of virial mass, M_{200} , for APOSTLE-L1 (solid red circles) haloes and their DMO counterparts (open red circles), and Aquarius haloes (open stars). The results from EAGLE L0250752-Ref and its DMO counterpart are shown using small solid green circles and grey open circles, respectively. The prediction of Wang et al. (2012, W12) with 1σ scatter is shown by the grey band. Including the 12 per cent reduction in V_{\max} brings the W12 relation down to the green dotted line. The horizontal dashed line indicates the number of MW satellites brighter than $M_V = -8$. *Bottom:* The fraction of haloes with 12 or fewer massive subhaloes (i.e., $V_{\max} > 25 \text{ km s}^{-1}$), as a function of the virial mass of the primary. The grey curve corresponds to the Wang et al. (2012) estimate from dark-matter-only simulations. The green curve includes the 12 per cent reduction in V_{\max} obtained in hydrodynamical simulations.

tion physics modules from the EAGLE project¹⁰. The offset between green and grey circles demonstrates the effect of the reduction of V_{\max} caused by the inclusion of baryons in the simulation.

The six Aquarius haloes (Springel et al. 2008) are shown by starred symbols: these systems are slightly overabundant in massive substructures relative to both the EAGLE runs and the predictions of Wang et al. (2012), which are based on large samples of haloes from the Millennium Simulations. Three Aquarius haloes have more than 12 massive substructures, and therefore would not be consistent

with the MW satellite population according to our APOSTLE results.

Including baryons changes this, as shown by the six primaries in APOSTLE L1: these are shown in Fig. 8 with red circles; filled symbols for the hydrodynamical runs, and open symbols for the DMO versions. The DMO runs give results similar to Aquarius: half of APOSTLE DMO are above the ‘MW’ line. The number of massive substructures drops substantially once baryons are included (filled circles), so that all six primaries in the APOSTLE L1 hydrodynamical runs are actually consistent with the MW.

We may use these results to derive firm upper limits on the mass of the Milky Way. This is shown in the bottom panel of Fig. 8 where each curve traces the fraction of haloes of a given virial mass that have 12 (or fewer) massive substructures (i.e., the observed number of Galactic satellites brighter than $M_V = -8$). We show results for two cases; one where the numbers are derived from the formula of Wang et al. (2012), assuming Poisson statistics (solid grey lines) and another where the zero-point of that relation has been shifted to account for the 12 per cent reduction in V_{\max} discussed above (see green dotted line in the top panel of Fig. 8).

Clearly, the reduction in V_{\max} induced by the loss of baryons in hydrodynamical simulations significantly relaxes the constraints based on dark-matter-only simulations. Indeed, according to this argument, fewer than 5 per cent of haloes more massive than $2.8 \times 10^{12} M_{\odot}$ can host the Milky Way, assuming the DMO relation. The same criterion results in an increased mass limit of $4.2 \times 10^{12} M_{\odot}$ adopting the V_{\max} correction. This may also be compared with the earlier analysis of Wang et al. (2012), which found an upper limit of $2 \times 10^{12} M_{\odot}$, and of Cautun et al. (2014), which derived an even stricter limit, albeit using slightly different criteria.

4 SUMMARY AND CONCLUSIONS

We use the APOSTLE suite of Λ CDM cosmological hydrodynamical simulations of the Local Group to examine the masses of satellite galaxies brighter than $M_V = -8$ (i.e., $M_{\text{str}} > 10^5 M_{\odot}$). Our analysis extends that of Sawala et al. (2016), where we showed that our simulations reproduce the Galactic satellite luminosity function and show no sign of either the ‘missing satellites’ problem nor of the ‘too-big-to-fail’ problem highlighted in earlier work. Our main conclusions may be summarised as follows.

Previous studies have underestimated the uncertainty in the mass enclosed within the half-light radii of Galactic dSphs, derived from their line-of-sight velocity dispersion and half-light radii. Our analysis takes into account the error propagation due to uncertainties in the distance, effective radius, and velocity dispersion, and also include an estimate of the intrinsic dispersion of the modeling procedure, following the recent work of Campbell et al. (2016). The latter is important as it introduces a base systematic uncertainty that exceeds ~ 20 per cent.

Simulated galaxies in APOSTLE/EAGLE follow a stellar mass – halo mass relation that differs, for dwarf galaxies, from common extrapolations of abundance matching models, a difference that is even more pronounced for satellites

¹⁰ This simulation is labelled L0250752 in Schaye et al. (2015) and was run using the parameters of the ‘Ref’ model.

due to tidal stripping, At fixed stellar mass, APOSTLE dwarfs inhabit halos significantly less massive than AM predicts. This difference, however, might not be readily apparent because tides strip halos from the outside in and some dSphs are too compact for tidal effects to be readily apparent.

We find that the dynamical mass of *all* Galactic dSphs is in excellent agreement with that of APOSTLE satellites that match their stellar mass. APOSTLE centrals (i.e., not satellites), on the other hand, overestimate the observed mass of four Galactic dSphs (Can Ven I, Sextans, Carina, and Fornax), suggesting that they have had their dark matter content significantly reduced by stripping. The other, more compact, dSphs are well fit by either APOSTLE satellites or centrals, so tides are not needed to explain their dark matter content.

After accounting for tidal mass losses, we find that all APOSTLE halos (satellites or centrals) with $V_{\max} > 25 \text{ km s}^{-1}$ host dwarfs brighter than $M_V = -8$. Only systems with fewer than ~ 12 subhaloes with $V_{\max} > 25 \text{ km/s}$ are thus compatible with the population of luminous MW satellites. This suggests an upper limit to the mass of the Milky Way halo: we find that most halos with virial mass not exceeding $2 \times 10^{12} M_{\odot}$ should pass this test, unless they are unusually overabundant in massive substructures.

Our APOSTLE primaries satisfy these constraints, and show a dwarf galaxy population in agreement with observations of the Local Group, including their abundance as a function of mass, their dark matter content, and their global kinematics. Furthermore, APOSTLE uses the same galaxy formation model that was found by EAGLE to reproduce the galaxy stellar mass function in cosmologically significant volumes. We consider this a significant success for direct simulations of galaxy formation based on the Λ CDM paradigm.

We note that this success does not require any substantial modification to well-established properties of Λ CDM. In particular, none of our simulated dwarf galaxies have ‘cores’ in their dark mass profiles, but yet have no trouble reproducing the detailed properties of Galactic satellites. Baryon-induced cores are not mandatory to solve the ‘too-big-to-fail’ problem.

We end by noting that a number of recent studies have argued that TBTF-like problems also arise when considering the properties of M31 satellites (Tollerud et al. 2014; Collins et al. 2014), as well as those of field galaxies in the local Universe (Garrison-Kimmel et al. 2014; Papastergis et al. 2015). It remains to be seen whether the resolution we advocate here for Galactic satellites will solve those problems as well. We plan to report on those issues in future work.

5 ACKNOWLEDGEMENTS

We acknowledge useful discussions with Mike Boylan-Kolchin, Manolis Papastergis, and Alan McConnachie. The research was supported in part by the Science and Technology Facilities Council Consolidated Grant (ST/F001166/1), and the European Research Council under the European Unions Seventh Framework Programme (FP7/2007-2013)/ERC Grant agreement 278594-

GasAroundGalaxies. CSF acknowledges ERC Advanced Grant 267291 COSMIWAY; and JW the 973 program grant 2015CB857005 and NSFC grant No. 11373029, 11390372. This work used the DiRAC Data Centric system at Durham University, operated by the Institute for Computational Cosmology on behalf of the STFC DiRAC HPC Facility (www.dirac.ac.uk), and also resources provided by WestGrid (www.westgrid.ca) and Compute Canada (www.computecanada.ca). The DiRAC system was funded by BIS National E-infrastructure capital grant ST/K00042X/1, STFC capital grants ST/H008519/1 and ST/K00087X/1, STFC DiRAC Operations grant ST/K003267/1 and Durham University. DiRAC is part of the National E-Infrastructure. This research has made use of NASA’s Astrophysics Data System.

REFERENCES

- Barber, C., Starkenburg, E., Navarro, J. F., McConnachie, A. W., & Fattahi, A. 2014, *MNRAS*, 437, 959
- Behroozi, P. S., Marchesini, D., Wechsler, R. H., et al. 2013, *ApJ*, 777, L10
- Benson, A. J., Lacey, C. G., Baugh, C. M., Cole, S., & Frenk, C. S. 2002, *MNRAS*, 333, 156
- Boylan-Kolchin, M., Bullock, J. S., & Kaplinghat, M. 2011, *MNRAS*, 415, L40
- . 2012, *MNRAS*, 422, 1203
- Brooks, A. M., & Zolotov, A. 2014, *ApJ*, 786, 87
- Bullock, J. S., Kravtsov, A. V., & Weinberg, D. H. 2000, *ApJ*, 539, 517
- Campbell, D. J. R., Frenk, C. S., Jenkins, A., et al. 2016, *ArXiv e-prints*, arXiv:1603.04443
- Cautun, M., Frenk, C. S., van de Weygaert, R., Hellwing, W. A., & Jones, B. J. T. 2014, *MNRAS*, 445, 2049
- Collins, M. L. M., Chapman, S. C., Rich, R. M., et al. 2014, *ApJ*, 783, 7
- Crain, R. A., Schaye, J., Bower, R. G., et al. 2015, *MNRAS*, 450, 1937
- Davis, M., Efstathiou, G., Frenk, C. S., & White, S. D. M. 1985, *ApJ*, 292, 371
- Di Cintio, A., Brook, C. B., Macciò, A. V., et al. 2014, *MNRAS*, 437, 415
- Dolag, K., Borgani, S., Murante, G., & Springel, V. 2009, *MNRAS*, 399, 497
- Fattahi, A., Navarro, J. F., Sawala, T., et al. 2016, *MNRAS*, 457, 844
- Ferrero, I., Abadi, M. G., Navarro, J. F., Sales, L. V., & Gurovich, S. 2012, *MNRAS*, 425, 2817
- Frenk, C. S., White, S. D. M., Davis, M., & Efstathiou, G. 1988, *ApJ*, 327, 507
- Garrison-Kimmel, S., Boylan-Kolchin, M., Bullock, J. S., & Lee, K. 2014, *MNRAS*, 438, 2578
- Garrison-Kimmel, S., Rocha, M., Boylan-Kolchin, M., Bullock, J. S., & Lally, J. 2013, *MNRAS*, 433, 3539
- Governato, F., Zolotov, A., Pontzen, A., et al. 2012, *MNRAS*, 422, 1231
- Guo, Q., Cole, S., Eke, V., & Frenk, C. 2011, *MNRAS*, 417, 370
- Guo, Q., Cooper, A. P., Frenk, C., Helly, J., & Hellwing, W. A. 2015, *MNRAS*, 454, 550

- Guo, Q., White, S., Li, C., & Boylan-Kolchin, M. 2010, MNRAS, 404, 1111
- Irwin, M., & Hatzidimitriou, D. 1995, MNRAS, 277, 1354
- Jenkins, A. 2013, MNRAS, 434, 2094
- Kirby, E. N., Bullock, J. S., Boylan-Kolchin, M., Kaplinghat, M., & Cohen, J. G. 2014, MNRAS, 439, 1015
- Klypin, A., Kravtsov, A. V., Valenzuela, O., & Prada, F. 1999, ApJ, 522, 82
- Koch, A., Kleyna, J. T., Wilkinson, M. I., et al. 2007, AJ, 134, 566
- Komatsu, E., Smith, K. M., Dunkley, J., et al. 2011, ApJS, 192, 18
- Martin, N. F., de Jong, J. T. A., & Rix, H.-W. 2008, ApJ, 684, 1075
- Mashchenko, S., Couchman, H. M. P., & Wadsley, J. 2006, Nature, 442, 539
- Mateo, M., Olszewski, E. W., & Walker, M. G. 2008, ApJ, 675, 201
- McConnachie, A. W. 2012, AJ, 144, 4
- Moore, B., Ghigna, S., Governato, F., et al. 1999, ApJ, 524, L19
- Moster, B. P., Naab, T., & White, S. D. M. 2013, MNRAS, 428, 3121
- Navarro, J. F., Eke, V. R., & Frenk, C. S. 1996a, MNRAS, 283, L72
- Navarro, J. F., Frenk, C. S., & White, S. D. M. 1996b, ApJ, 462, 563
- . 1997, ApJ, 490, 493
- Navarro, J. F., Ludlow, A., Springel, V., et al. 2010, MNRAS, 402, 21
- Oñorbe, J., Boylan-Kolchin, M., Bullock, J. S., et al. 2015, MNRAS, 454, 2092
- Oman, K. A., Navarro, J. F., Fattahi, A., et al. 2015, MNRAS, 452, 3650
- Palma, C., Majewski, S. R., Siegel, M. H., et al. 2003, AJ, 125, 1352
- Papastergis, E., Giovanelli, R., Haynes, M. P., & Shankar, F. 2015, A&A, 574, A113
- Parry, O. H., Eke, V. R., Frenk, C. S., & Okamoto, T. 2012, MNRAS, 419, 3304
- Peñarrubia, J., McConnachie, A. W., & Navarro, J. F. 2008a, ApJ, 672, 904
- Peñarrubia, J., Navarro, J. F., & McConnachie, A. W. 2008b, ApJ, 673, 226
- Pontzen, A., & Governato, F. 2014, Nature, 506, 171
- Power, C., Navarro, J. F., Jenkins, A., et al. 2003, MNRAS, 338, 14
- Sales, L. V., Navarro, J. F., Oman, K., et al. 2016, ArXiv e-prints, arXiv:1602.02155
- Sawala, T., Frenk, C. S., Crain, R. A., et al. 2013, MNRAS, 431, 1366
- Sawala, T., Frenk, C. S., Fattahi, A., et al. 2015, MNRAS, 448, 2941
- . 2016, MNRAS, 457, 1931
- Schaller, M., Dalla Vecchia, C., Schaye, J., et al. 2015a, MNRAS, 454, 2277
- Schaller, M., Frenk, C. S., Bower, R. G., et al. 2015b, MNRAS, 451, 1247
- Schaye, J., Crain, R. A., Bower, R. G., et al. 2015, MNRAS, 446, 521
- Simon, J. D., & Geha, M. 2007, ApJ, 670, 313
- Somerville, R. S. 2002, ApJ, 572, L23
- Springel, V. 2005, MNRAS, 364, 1105
- Springel, V., Yoshida, N., & White, S. D. M. 2001, New Astronomy, 6, 79
- Springel, V., Wang, J., Vogelsberger, M., et al. 2008, MNRAS, 391, 1685
- Tollerud, E. J., Boylan-Kolchin, M., & Bullock, J. S. 2014, MNRAS, 440, 3511
- Vale, A., & Ostriker, J. P. 2004, MNRAS, 353, 189
- Vera-Ciro, C. A., Helmi, A., Starkenburg, E., & Breddels, M. A. 2013, MNRAS, 428, 1696
- Walker, M. G., Mateo, M., Olszewski, E. W., et al. 2007, ApJ, 667, L53
- . 2009a, ApJ, 704, 1274
- Walker, M. G., Mateo, M., Olszewski, E. W., Sen, B., & Woodroffe, M. 2009b, AJ, 137, 3109
- Wang, J., Frenk, C. S., Navarro, J. F., Gao, L., & Sawala, T. 2012, MNRAS, 424, 2715
- Wolf, J., Martinez, G. D., Bullock, J. S., et al. 2010, MNRAS, 406, 1220
- Woo, J., Courteau, S., & Dekel, A. 2008, MNRAS, 390, 1453
- Zolotov, A., Brooks, A. M., Willman, B., et al. 2012, ApJ, 761, 71

This paper has been typeset from a $\text{\TeX}/\text{\LaTeX}$ file prepared by the author.

APPENDIX A: NUMERICAL CORRECTIONS

As discussed by Power et al. (2003), the enclosed mass profiles of N-body realizations of Λ CDM haloes converge outside a minimum radius, r_{conv} , that depends on the number of particles enclosed and on the mean inner density of the halo at that radius. This is because simulated profiles converge only for radii where the two-body relaxation timescale is long compared with the age of the Universe. A criterion for convergence may thus be derived using the ratio of relaxation time to the circular velocity at the virial radius:

$$\kappa(r) = \frac{t_{\text{relax}}(r)}{t_{\text{circ}}(r_{200})} = \frac{N(r)}{8 \ln N(r)} \frac{r/V_c}{r_{200}/V_{200}}, \quad (\text{A1})$$

which may also be written as,

$$\kappa(r) = \frac{\sqrt{200}}{8} \frac{N(r)}{\ln N(r)} \left(\frac{\bar{\rho}(r)}{\rho_{\text{crit}}} \right)^{-1/2}. \quad (\text{A2})$$

where $N(r)$ is the enclosed number of particles and $\bar{\rho}(r)$ is the mean density inside the radius r . At radii where $\kappa \approx 1$ profiles converge to better than 10 per cent in terms of circular velocity. Stricter convergence demands larger values of κ and implies, consequently, larger values of r_{conv} (Navarro et al. 2010).

Fig. A1 illustrates this for the case of the dark-matter-only realizations of four different APOSTLE primary haloes, run at three different resolutions, each differing by about a factor of ~ 10 in particle mass and ~ 2 in force resolution (L1 to L3, where L1 is best resolved).

The left panel of Fig. A1 shows the mean enclosed density at various radii. Different colours indicate the various resolution levels, whereas different symbols correspond to different haloes. At large radii all resolutions converge to the same result (i.e., like symbols line up horizontally). At small

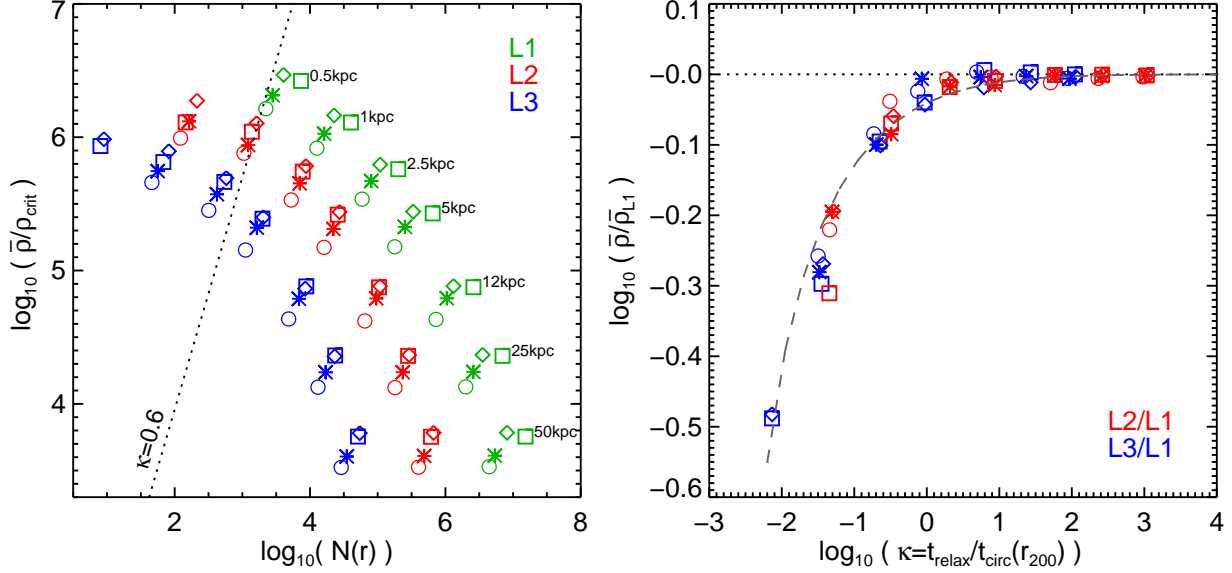


Figure A1. *Left:* Mean inner density as a function of enclosed number of particles at different radii, as labelled, for 4 primary haloes in dark-matter-only APOSTLE, simulated at three different resolution levels (L1 to L3). Different haloes are shown by different symbols, and colours indicate different resolution levels. Points to the right of the $\kappa = 0.6$ line (eq. A2) converge in circular velocity to better than 15 per cent (Power et al. 2003). Two L3 haloes have fewer than 5 particles at the smallest radius, and are not shown. *Right:* Mean inner density as a function of κ for L2 and L3 haloes, normalized to the values obtained for the highest-resolution run, L1. Symbols are the same as in the left panel. The dashed line has been used to correct densities at small radii.

radii, however, the lower-resolution profiles gradually deviate from the highest-resolution (L1) run. The Power et al. (2003) criterion is shown by the inclined dotted line, for $\kappa = 0.6$. Note that points clearly converge, regardless of resolution, to the right of this line, but those on the left deviate noticeably from the results obtained for the highest-resolution case, L1.

The smooth trend in density contrast with enclosed particle number suggests a simple way to correct an under-resolved halo profile. Indeed, expressed in terms of κ , the ‘deficit’ in density observed in the inner regions always follows the same pattern. This is shown in the right-hand panel of Fig. A1, where we show, for all radii ≥ 0.5 kpc and all haloes, the density in units of the ‘true’ values obtained for L1. All haloes follow the same pattern, which we approximate with a fitting function, $\log(1 - \bar{\rho}/\bar{\rho}_{\text{conv}}) = a(\log \kappa)^2 + b(\log \kappa) + c$ where $(a, b, c) = (-0.04, -0.5, -1.05)$.

Since densities of L1 are ‘converged’ according to the left-hand panel of Fig. A1 ($\bar{\rho}_{L1} = \bar{\rho}_{\text{conv}}$), the aforementioned trend may be used to extrapolate the results of a simulation to radii smaller than the traditional value of r_{conv} dictated by assuming $\kappa = 0.6$.

We show in Fig. A2 the results of applying this correction to Sculptor-like central galaxies in APOSTLE-L1. Typical values of κ at $r_{1/2}$ for this galaxy are about 0.15, which results in a correction in enclosed density of roughly 20 per cent. The distribution shown in the right-hand panel of Fig. A2 is then used statistically to correct the raw $V_{1/2}$ estimates from our L1 satellites. The result of applying this to Sculptor-like satellites is shown in Fig. 5. This same procedure is applied separately to each Galactic satellite in order to derive the predictions shown in Fig. 6.

Table A1. The parameters of classical dSph satellites of MW.

name	$(m - M)_0$	R_{eff}	σ_{los}	m_V	$\frac{M_{\text{str}}}{L_V}$	3D $r_{1/2}$	$M_{1/2}$	$V_{1/2}$	M_{str}
		(arcmin)	(km s ⁻¹)			(pc)	(10 ⁷ M _⊙)	(km s ⁻¹)	(10 ⁶ M _⊙)
ref.	(a)			(a)	(b)				
For	20.84 ± 0.18	16.6 ± 1.2 ^{a,c}	11.7 ± 0.9 ^f	7.4 ± 0.3	1.2	950 ⁺⁷⁰⁽¹⁴⁰⁾ ₋₇₀₍₁₃₀₎	8.9 ^{+1.9(3.8)} _{-1.7(3.0)}	20.1 ± 1.9(3.6)	24 ⁺⁶⁽¹³⁾ ₋₅₍₉₎
Leo I	22.02 ± 0.13	3.4 ± 0.3 ^{a,c}	9.2 ± 1.4 ^g	10.0 ± 0.3	0.9	334 ⁺²⁴⁽⁴⁷⁾ ₋₂₄₍₄₄₎	1.9 ^{+0.6(1.2)} _{-0.6(0.8)}	15.8 ± 2.0(3.9)	5.0 ^{+1.1(2.4)} _{-1.0(1.7)}
Scl	19.67 ± 0.14	11.3 ± 1.6 ^{a,c}	9.2 ± 1.1 ^f	8.6 ± 0.5	1.7	377 ⁺⁴⁰⁽⁷⁷⁾ ₋₃₉₍₇₃₎	2.2 ^{+0.6(1.2)} _{-0.5(0.9)}	15.8 ± 1.8(3.4)	3.9 ^{+1.5(3.4)} _{-1.1(1.8)}
Leo II	21.84 ± 0.13	2.6 ± 0.6 ^{a,c}	6.6 ± 0.7 ^h	12 ± 0.3	1.6	235 ⁺³⁸⁽⁷³⁾ ₋₃₈₍₇₁₎	0.68 ^{+0.21(0.4)} _{-0.17(0.3)}	11.3 ± 1.2(2.3)	1.2 ^{+0.3(0.6)} _{-0.2(0.4)}
Sex I	19.67 ± 0.10	27.8 ± 1.2 ^{a,c}	7.9 ± 1.3 ^f	10.4 ± 0.5	1.6	926 ⁺⁴⁰⁽⁷⁷⁾ ₋₃₉₍₇₃₎	3.9 ^{+1.2(2.5)} _{-1.0(1.7)}	13.5 ± 1.9(3.5)	0.7 ^{+0.3(0.6)} _{-0.2(0.3)}
Car	20.11 ± 0.13	8.2 ± 1.2 ^{a,c}	6.6 ± 1.2 ^f	11.0 ± 0.5	1.0	334 ⁺³⁶⁽⁶⁹⁾ ₋₃₅₍₆₆₎	1.0 ^{+0.3(0.7)} _{-0.3(0.5)}	11.3 ± 1.7(3.1)	0.38 ^{+0.14(0.32)} _{-0.11(0.18)}
UMi	19.40 ± 0.10	19.9 ± 1.9 ^d	9.5 ± 1.2 ⁱ	10.6 ± 0.5	1.9	584 ⁺⁴²⁽⁸²⁾ ₋₄₁₍₇₈₎	3.6 ^{+1.0(2.0)} _{-0.8(1.4)}	16.3 ± 1.9(3.6)	0.54 ^{+0.21(0.46)} _{-0.15(0.25)}
Dra	19.40 ± 0.17	10.0 ^{+0.3,e} _{-0.2}	9.1 ± 1.2 ^j	10.6 ± 0.2	1.8	294 ⁺¹⁷⁽³³⁾ ₋₁₆₍₃₀₎	1.7 ^{+0.5(0.9)} _{-0.4(0.7)}	15.6 ± 1.9(3.6)	0.51 ^{+0.09(0.20)} _{-0.09(0.15)}
CVn I	21.69 ± 0.10	8.9 ± 0.4 ^e	7.6 ± 0.4 ^k	13.1 ± 0.2	1.6	751 ⁺³⁴⁽⁶⁴⁾ ₋₃₂₍₆₀₎	3.0 ^{+0.5(1.1)} _{-0.5(0.9)}	13.1 ± 1.1(2.1)	0.37 ^{+0.06(0.13)} _{-0.05(0.10)}

Notes: Uncertainties in the observed parameters are taken directly from the references. We assume in all cases that they correspond to standard deviations of a Gaussian error distribution. The uncertainties quoted for derived parameters, i.e. the last four columns, correspond to interquartile and 10–90th percentile intervals, written outside and inside parentheses, respectively.

References: ^aMcConnachie (2012); ^bWoo et al. (2008); ^cIrwin & Hatzidimitriou (1995); ^dPalma et al. (2003); ^eMartin et al. (2008); ^fWalker et al. (2009b); ^gMateo et al. (2008); ^hKoch et al. (2007); ⁱWalker et al. (2009a); ^jWalker et al. (2007); ^kSimon & Geha (2007).

Table A2. Parameters of APOSTLE satellites matching the stellar mass of Galactic classical dSph satellites.

	$M_{1/2}$	$V_{1/2}$	V_{max}
	(10 ⁷ M _⊙)	(km s ⁻¹)	(km s ⁻¹)
Fornax-like (14)	13 ⁺³⁽⁶⁾ ₋₃₍₅₎	25.5 ^{+1.8(3.4)} _{-4.0(5.1)}	23.0 ^{+4.6(4.6)} _{-0(3.07)}
Leo I-like (37)	2.0 ^{+0.5(1.0)} _{-0.5(0.8)}	16.2 ^{+1.5(3.1)} _{-1.7(3.3)}	24.7 ^{+2.6(6.7)} _{-4.1(6.5)}
Sculptor-like(56)	2.1 ^{+0.8(1.6)} _{-0.6(1.2)}	15.7 ^{+2.0(4.0)} _{-1.9(4.4)}	23.0 ^{+4.2(5.5)} _{-4.6(5.7)}
Leo II-like(50)	0.9 ^{+0.5(1.0)} _{-0.4(0.6)}	12.8 ^{+2.3(4.4)} _{-2.4(4.6)}	17.7 ^{+4.0(6.6)} _{-3.5(4.5)}
Sextans-like(89)	7.1 ^{+2.7(4.2)} _{-2.3(4.6)}	18.2 ^{+3.0(4.4)} _{-3.4(7.4)}	14.2 ^{+1.2(4.1)} _{-1.1(3.8)}
Carina-like(117)	1.4 ^{+0.6(1.2)} _{-0.5(0.8)}	13.8 ^{+2.0(3.9)} _{-3.0(4.7)}	14.0 ^{+3.2(8.0)} _{-3.7(4.5)}
Ursa Minor-like(95)	3.7 ^{+1.2(2.4)} _{-1.1(2.3)}	16.6 ^{+2.6(4.1)} _{-4.2(5.7)}	19.8 ^{+2.2(4.0)} _{-4.3(5.6)}
Draco-like(48)	1.3 ^{+0.4(0.8)} _{-0.4(0.8)}	14.7 ^{+1.9(3.1)} _{-1.7(5.1)}	21.3 ^{+1.9(4.1)} _{-2.5(6.0)}
Canes Venatici I-like(45)	5.3 ^{+2.0(3.0)} _{-2.6(3.4)}	17.6 ^{+2.9(4.1)} _{-5.2(7.2)}	11.7 ^{+2.8(3.8)} _{-1.2(1.8)}

Notes: Values of $M_{1/2}$ and $V_{1/2}$ have been corrected by the procedure outlined in Appendix A. V_{max} values are obtained by matching the stellar mass and $V_{1/2}$ of APOSTLE satellites to those of MW satellites. See text for details. Numbers quoted in parentheses after the names are the number of simulated satellites matching the stellar mass of the corresponding MW dSph. Similar to Table A1, uncertainties represent interquartile and 10–90th percentile intervals, written outside and inside parentheses, respectively.

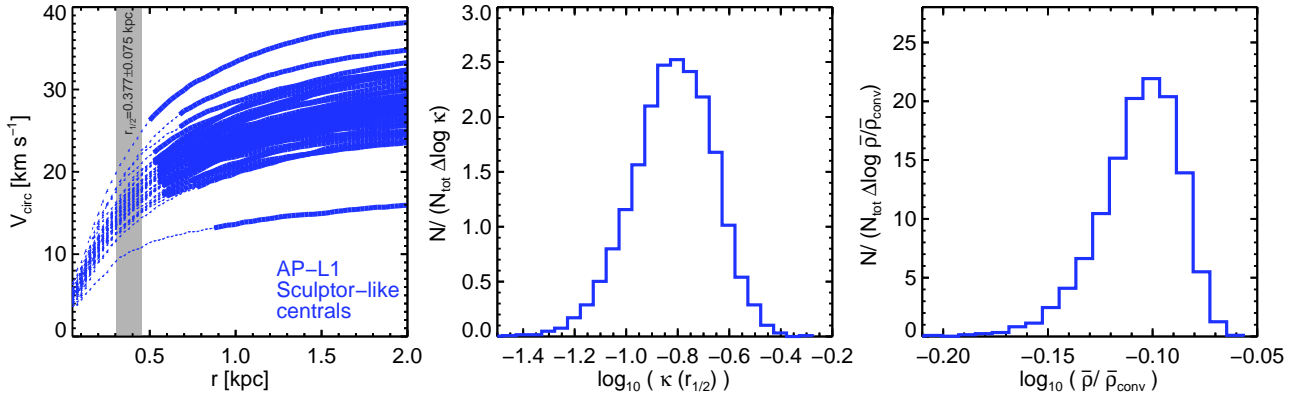


Figure A2. *Left:* Circular velocity curves of Sculptor-like APOSTLE centrals. The grey band corresponds to the 10–90th percentile interval for the observed $r_{1/2}$ of Sculptor. *Middle:* Distribution of $\kappa(r) = t_{\text{relax}}(r)/t_{\text{circ}}(r_{200})$ for the rotation curves in the left panel, at radii consistent with the $r_{1/2}$ of Sculptor. *Right:* Distribution of the density correction factor derived from the κ distribution of the middle panel and the fit presented in the right panel of Fig. A1.